OPEN ACCESS
Journal of Innovative Optical Health Sciences
Vol. 16, No. 2 (2023) 2244003 (11 pages)

DOI: 10.1142/S1793545822440035

World Scientific
www.worldscientific.com

Automated apoptosis identification in fluorescence imaging of nucleus based on histogram of oriented gradients of high-frequency wavelet coefficients

Shutong Liu[*,†], Limei Su[*,†], Han Sun[*,†], Tongsheng Chen[*,†,§], Min Hu[‡,¶] and Zhengfei Zhuang[*,†,‖]

[*]*MOE Key Laboratory of Laser Life Science and Institute of Laser Life Science College of Biophotonics, South China Normal University Guangzhou 510631, P. R. China*

[†]*Guangdong Provincial Key Laboratory of Laser Life Science College of Biophotonics, South China Normal University Guangzhou 510631, P. R. China*

[‡]*Guangdong Provincial Key Laboratory of Nanophotonic Functional Materials and Devices School of Information and Optoelectronic Science and Engineering South China Normal University Guangzhou 510631, P. R. China*

[§]*SCNU Qingyuan Institute of Science and Technology Innovation Co., Ltd. Qingyuan 511500, P. R. China*

[¶]*hmin@scnu.edu.cn*

[‖]*zhuangzf@scnu.edu.cn*

Received 18 March 2022
Accepted 5 June 2022
Published 30 August 2022

The automatic and accurate identification of apoptosis facilitates large-scale cell analysis. Most identification approaches using nucleus fluorescence imaging are based on specific morphological parameters. However, these parameters cannot completely describe nuclear morphology, thus limiting the identification accuracy of models. This paper proposes a new feature extraction method to improve the performance of the model for apoptosis identification. The proposed method uses a histogram of oriented gradient (HOG) of high-frequency wavelet coefficients to extract internal and edge texture information. The HOG vectors are classified using support vector machine. The experimental results demonstrate that the proposed feature extraction method well performs apoptosis identification, attaining 95.7% accuracy with low cost in terms of time. We confirmed that our method has potential applications to cell biology research.

Keywords: Apoptosis; nucleus; fluorescence imaging; HOG; wavelet decomposition.

[¶]Corresponding author.

1. Introduction

Apoptosis is an ordered and coordinated cellular process occurring under both physiological and pathological conditions; it is one of the topics most studied by cell biologists.[1] The morphological characteristics of apoptosis in the nucleus are chromatin condensation and nuclear fragmentation accompanied by cell rounding, reduction in cellular volume (pyknosis), and retraction of pseudopods.[2] Chromatin condensation begins at the periphery of the nuclear membrane, forming a crescent or ring-like structure. Inside a cell with an intact membrane, condensation continues until chromatin breaks up; this feature is called as karyorrhexis.[3] In recent years, the automated high-content screening (HCS) platform has been developed and applied to the screening of apoptosis-related drugs and cell biology research.[4–6] A rapid and accurate automatic identification method for apoptosis can greatly reduce the interaction between the operator and HCS imaging system, improving the efficiency of large-scale cell analysis.[7]

Over the years, machine learning and deep learning technologies have exhibited remarkable performance in biomedical image classification.[8–10] In particular, MobileNet,[11] AlexNet,[12] ResNet,[13] local binary pattern (LBP),[14] and gray-level co-occurrence matrix (GLCM)[15] have achieved desirable identification performance levels and have been adopted for various biomedical imaging tasks. Many researchers have designed algorithms specifically for apoptosis identification. For example, Mobiny *et al.* used a capsule network in phase-contrast microscopy to extract the edge and internal texture of cells for apoptosis classification.[16] Feng *et al.* used four classifiers with all the attributes or active attributes of GLCM to identify apoptosis in diffraction images.[17]

Previous studies on apoptosis classification or identification in nucleus fluorescence imaging were mainly based on manually extracted features. For example, a specified threshold of mean intensity is used to distinguish between apoptotic and healthy cells.[18] However, uneven illumination intensities can easily affect this method, and the threshold setting is not universal. A more advanced method selects nuclear morphological parameters (such as cell stain intensity (e.g., using CellTracker dyes), size, and roundness) as feature vectors.[19,20] Binary trees[21] or other classifiers have been employed for classification. However, manually assigned morphological parameters cannot fully reflect the morphological characteristics of the nucleus, thus affecting the final prediction.

This paper proposes a method based on the histogram of oriented gradients (HOGs) of high-frequency wavelet coefficients to identify apoptotic cells in nucleus fluorescence imaging. The use of HOGs instead of typical morphological parameters enables the more complete description of the representation and shape of local objects. Furthermore, the method extracts HOGs by cells and normalizes features by blocks (Sec. 2.4.2),[22] eliminating the influence of uneven lighting and contrast. Before HOG extraction was implemented, wavelet decomposition was applied to the image to separate the high-frequency texture into horizontal, vertical, and diagonal directions.[23] This significantly reduces the HOG feature dimension and improves prediction accuracy.

2. Materials and Methods

2.1. *Cell culture and apoptosis induction*

The MCF7 human breast cancer cell line, obtained from the Department of Medicine, the Jinan University in China, was cultured in Dulbecco's modified Eagle's medium (Gibco, Grand Island, New York) containing 10% fetal calf serum (Sijiqing, Hangzhou, China) at 37°C and 5% CO_2 in a humidified incubator. When the cells confluence reached 70–90% in a 35 mm glass dish, the MCF7 cell line was treated with staurosporine (Sigma-Aldrich, Santa Clara, USA) at a concentration of 1 μmol/L for 6 h to induce apoptosis; untreated cells were used as controls. The nuclei were stained with Hoechst 33258 (Invitrogen, USA) for 15 min.

2.2. *Image acquisition*

The cells were monitored in fluorescent mode, and images were captured using a wide-field microscope (Observer.D1, Carl Zeiss, Germany), equipped with a high numerical objective (40×/1.3 NA Oil, Carl Zeiss, Germany) and an sCMOS camera (Flash 4.0, Hamamatsu, Japan); the excitation and emission wavelengths were 405 nm and 445 nm, respectively. The size of the raw captured image was 2048 × 2048 pixels.

2.3. *Image preprocessing and dataset establishment*

Image preprocessing included image normalization and image denoising. For image normalization, linear function mapping was applied. The corresponding relationship between the normalized image (y) and raw image (x) is as follows:

$$y = \frac{x - \min(x)}{\max(x) - \min(x)}. \quad (1)$$

To reduce noise, the normalized images were smoothed by a 3×3 Gaussian filter.

The adaptive threshold segmentation method, Otsu,[24] was implemented to segment the nucleus and crop single-nucleus patches around the centroid. We acquired 3500 nucleus patches of healthy and apoptotic samples. The ratio of healthy to apoptotic images in the dataset is 1:1. Each nucleus patch was manually annotated by a binary label ('0' for healthy and '1' for apoptotic). Additionally, bilinear interpolation was applied to transform the patches into 200×200 sizes. Performance was measured using 10-fold cross-validation in which the training and test sets were selected from different dishes to ensure independence. Because the HOG feature had no rotation invariance,[22] the training set images were rotated by 45°, 90°, 135°, 180°, 225°, 270°, and 315° to improve training; a total of 25,200 samples were used for training. The flowchart of image preprocessing and dataset establishment is shown in Fig. 1.

2.4. *Feature extraction and classification*

After establishing the dataset, image feature extraction and classification were implemented. The use of appropriate image features can significantly reduce the training time and improve prediction accuracy. Our proposed method first uses wavelet decomposition to obtain the horizontal, vertical, and diagonal wavelet coefficients (H, V, and D, respectively) and then extracts HOG feature vectors X_H, X_V, and X_D from the wavelet coefficients, respectively. After connecting X_H, X_V, and X_D in series, the final feature vector, X_{HVD}, is obtained. Finally, the final feature vectors are dropped into the support vector machine (SVM)[25] classifier for training and classifying. The flowchart of feature extraction and classification is shown in Fig. 2.

2.4.1. *Wavelet decomposition*

As an image analysis tool, wavelet decomposition can separate the image into a set of frequency channels with optional directions that are typically used in image texture identification, edge detection, and denoising. In this study, Mallat algorithm[26] was applied to first-order wavelet decomposition for

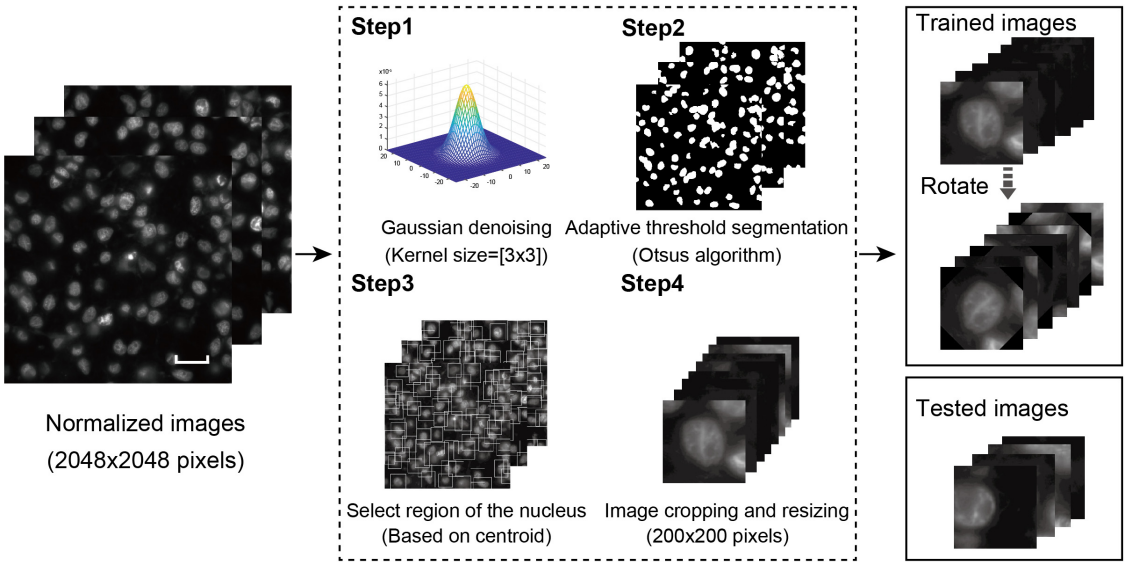

Fig. 1. Flowchart of image preprocessing and dataset establishment. Gaussian denoising was first performed on normalized image. Then, Otsu adaptive threshold method was applied for nuclear region segmentation. Rectangular region of nucleus was cropped and transformed to 200×200 pixels. Cropped images are rotated and added to dataset. Scale bar: 50 μm.

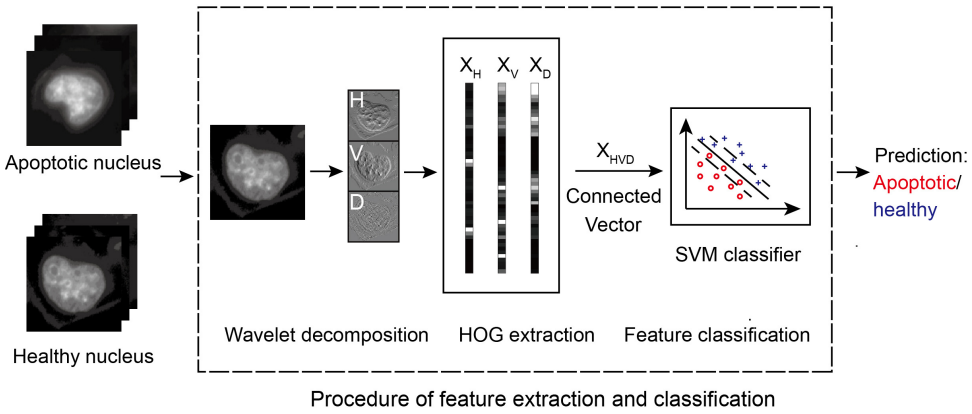

Fig. 2. Schematic of feature extraction and classification. First, image was decomposed to obtain high-frequency wavelet coefficients (H, V, and D). Then, HOG feature vectors X_H, X_V, and X_D were extracted and then connected in series to obtain final feature vector X_{HVD}. Finally, SVM classifier was used for feature classification.

effectively reducing the complexity of wavelet transform. Mallat's two-dimensional wavelet decomposition formula is defined as follows:

$$\begin{cases} c_{k,n}^{J+1} = \sum_l \sum_n c_{l,n}^J L(l-2k)L(n-2m), \\ d_{k,m}^{J+1,h} = \sum_l \sum_n c_{l,n}^J L(l-2k)H(n-2m), \\ d_{k,m}^{J+1,v} = \sum_l \sum_n c_{l,n}^J H(l-2k)L(n-2m), \\ d_{k,m}^{J+1,d} = \sum_l \sum_n c_{l,n}^J H(l-2k)H(n-2m), \end{cases} \quad (2)$$

where k is the row subscript; m is the column subscript; l and n are translation factors; J represents the decomposition level; H represents a high-pass filter function; and L represents a low-pass filter function. After the wavelet J decomposition of C^J, low-frequency (C^{J+1}), horizontal high-frequency ($d^{J+1,h}$), vertical high-frequency ($d^{J+1,v}$), and diagonal high-frequency ($d^{J+1,d}$) coefficients were obtained and simplified as A, H, V, and D, respectively. To achieve optimal classification results, the discrete Haar high-pass filter operator [−1,1] and low-pass filter operator [1,1] were used for wavelet decomposition. The wavelet decomposition results are shown in Fig. 3.

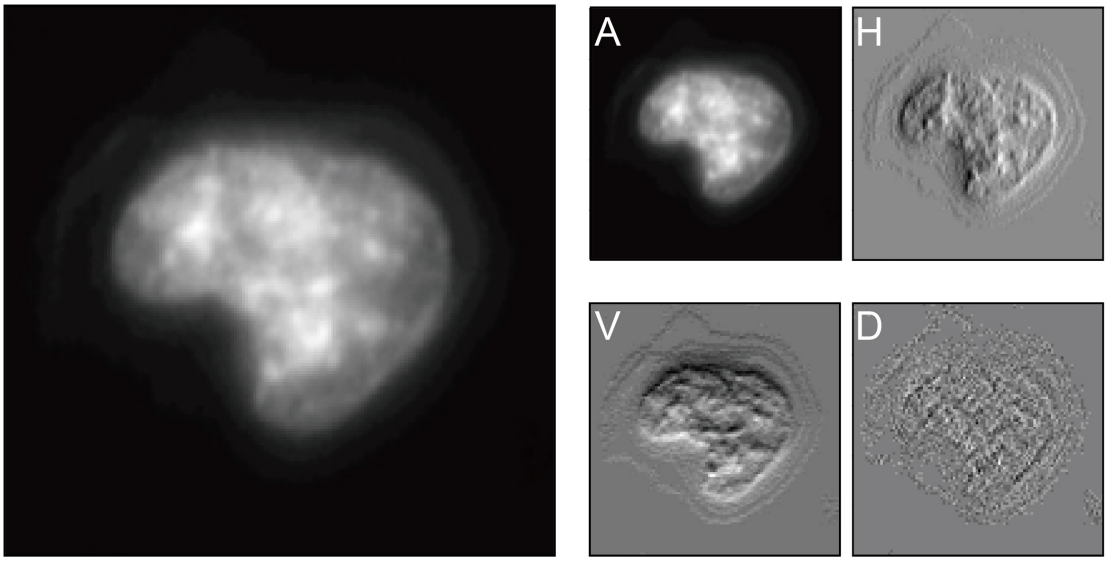

(a) (b)

Fig. 3. Wavelet decomposition results of nucleus image. (a) Resized image of apoptotic nucleus. (b) Low-frequency (A) and high-frequency horizontal (H), vertical (V), and diagonal (D) coefficients obtained by first-order wavelet decomposition.

2.4.2. *HOG feature extraction of high-frequency wavelet*

The appearance of apoptotic and healthy cells differs; nevertheless, because HOG can describe cell nucleus texture and edge orientation, it can identify apoptotic cells. The extraction process is as follows.

If the gray value of the image at (x, y) is assumed as $F(x, y)$, then the horizontal gradient, $G_x(x, y)$, and vertical gradient, $G_y(x, y)$, are defined as follows:

$$\begin{aligned} G_x(x, y) &= F(x + 1, y) - F(x - 1, y), \\ G_y(x, y) &= F(x, y + 1) - F(x, y - 1). \end{aligned} \tag{3}$$

The gradient amplitude, $G(x, y)$, and gradient direction angle, $\text{Angle}(x, y)$, are mathematically expressed as follows:

$$\begin{aligned} G_x(x, y) &= \text{sqrt}G_x(x, y)^2 + G_y(x, y)^2, \\ \text{Angle}(x, y) &= \tan^{-1}\frac{G_y(x, y)}{G_x(x, y)}. \end{aligned} \tag{4}$$

As shown in Fig. 4, a gradient amplitude image was obtained after calculating the gradient amplitude of each point in the image. Because directly extracting the gradient amplitude from the raw images could not reflect the complete shape of the nucleus edge and texture of holes in the nucleus, the raw image was decomposed by a wavelet. Then, the gradient amplitudes of the horizontal, vertical, and diagonal high-frequency coefficients were determined. The nucleus edge was observed to be missing over a large area in the gradient amplitude of the raw image. The texture of holes inside the nucleus was fuzzy and indistinct (Figs. 4(a) and 4(b)). However, the nucleus edges in the gradient amplitude of high-frequency wavelet coefficients are more continuous and clearer. In reality, removing the low-frequency while retaining the high-frequency coefficient is equivalent to enhancing the gray value of edge points and inhibiting nonedge points, which increases the gradient amplitude of the edge. The horizontal and vertical high-frequency gradient amplitudes (Figs. 4(a1) and 4(a2)) can extract the horizontal and vertical hole textures of the nucleus, respectively. Many long holes were present in the apoptotic nucleus, whereas many round holes were observed in the healthy nucleus (Figs. 4(b1) and 4(b2)). The diagonal high-frequency gradient

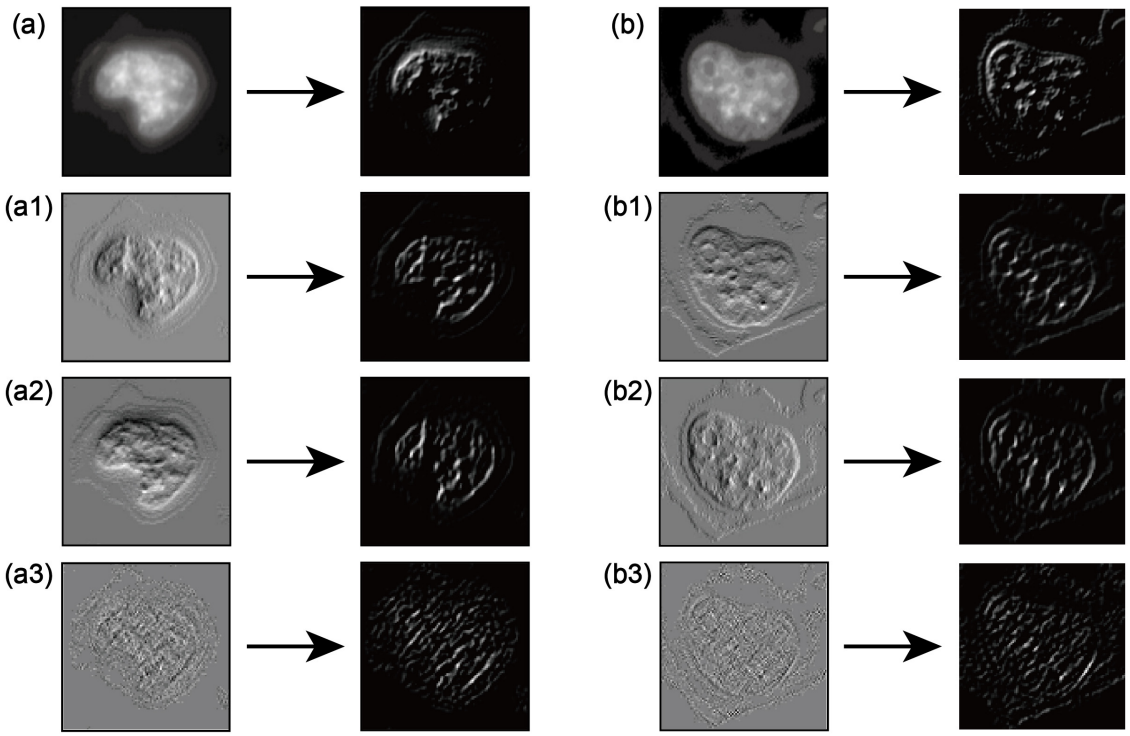

Fig. 4. Gradient amplitude of nucleus. (a) Resized raw image of apoptotic nucleus and its gradient amplitude image: (a1) horizontal, (a2) vertical, and (a3) diagonal high-frequency coefficients of apoptotic nucleus and its gradient amplitude image. (b) Resized raw image of healthy nucleus and its gradient amplitude image: (b1) horizontal, (b2) vertical, and (b3) diagonal high-frequency coefficients of healthy nucleus and its gradient amplitude image.

amplitude (Figs. 4(a3) and 4(b3)) reflects the overall diagonal texture of the cells. The healthy nucleus (Fig. 4(b3)) had clear edge contours. In contrast, the apoptotic nucleus (Fig. 4(a3)) showed blurry edges; hence, distinguishing the shape of the nucleus was difficult. After extracting the gradient from the high-frequency wavelet coefficient in the three directions, the amplitude and direction of the gradient were statistically analyzed.

The gradient image was divided into multiple rectangular $n \times n$ windows (cells), and the histograms of oriented gradients of the cell region were counted. The statistical method is as follows: the gradient directions $[-90°, 90°]$ are divided into a specific number of intervals (bins), i.e., nine. The amplitude formula of the pixel point (x, y) in interval k is as follows:

$$N_k = \begin{cases} G(x,y), & \text{Angle} \in (\text{bin}_k), \\ 0, & \text{Angle} \notin (\text{bin}_k). \end{cases} \quad (5)$$

The sum of the amplitudes of all pixels in the cell was counted in different bins to obtain the cell histogram vector. The vectors of all the cell regions were connected in series to obtain the HOG feature vector of the entire image.

To eliminate the influence of image region contrast and uneven illumination on the gradient amplitude, we normalized the HOG feature vectors in the local area (block). The block in this study was set as a rectangle containing $m \times m$ cell windows; the $L2$ norm was used for normalization.

2.4.3. *Classifier*

The SVM was used for feature classification because of the small sample size, considerable feature variations within the sample class, and tendency of data characteristic overfitting.[27] The SVM uses a kernel function to map feature vectors into a high-dimensional feature space and then implements hyperplane fitting. The commonly used kernel functions are linear, polynomial, and radial basis function (RBF) kernels. The RBF kernel is used in this study and defined as follows:

$$K(x,y) = \exp^{\frac{-\|x-1\|^2}{2\sigma^2}}. \quad (6)$$

3. Experimental Results

3.1. *Training methods and evaluation indices*

In this study, the models were trained 10 times on random subsets of the original dataset. Prediction accuracy, precision, recall, $F1$-score, subject area under the operating curve (AUC), and other sample parameters in the test set were used as evaluation indices. Note that the samples obtained from the same dishes are only allowed to be used together in the training set or together in the test set.

3.2. *Parameter comparison experiment*

3.2.1. *Comparison of prediction performance with HOG feature combination modes*

After wavelet decomposition, the high-frequency coefficients in the three directions were obtained. Different high-frequency HOG feature combination modes were selected to evaluate the performance in terms of prediction accuracy. Two typical feature combination modes are shown in Figs. 5(a) and 5(b). A tandem feature combination mode in which the HOG features of the high-frequency coefficient in all directions are connected in series to obtain the final feature vector is shown in Fig. 5(a). The overlay combination mode is shown in Fig. 5(b). The HOG features were extracted from the superimposed high-frequency coefficients. Superimposed images are frequently used for wavelet denoising and image reconstruction.[28] The average prediction accuracy is shown in Fig. 5(c). The result shows that models with low-frequency coefficients have a lower prediction accuracy (between 84.6% and 93.4%, with an average of 88.6%) than the models removing low-frequency coefficients (between 92.7% and 95.7%, with an average of 94.40%). Overall, the tandem feature combination mode can obtain high prediction accuracy. Specifically, the final feature vector, X_{HVD}, obtained by connecting high-frequency X_H, X_V, and X_D HOG feature vectors in series yields a model with the highest prediction accuracy.

3.2.2. *Parameter optimization during HOG feature extraction*

The effect of HOG feature extraction is mainly influenced by the sizes of the cell window and block region of the normalized gradient amplitude. The cell window size determines the texture size or edge morphological features that we focus on. This affects the final prediction accuracy and feature vector dimension; the latter influences the model training time, which is measured by CPU running time from

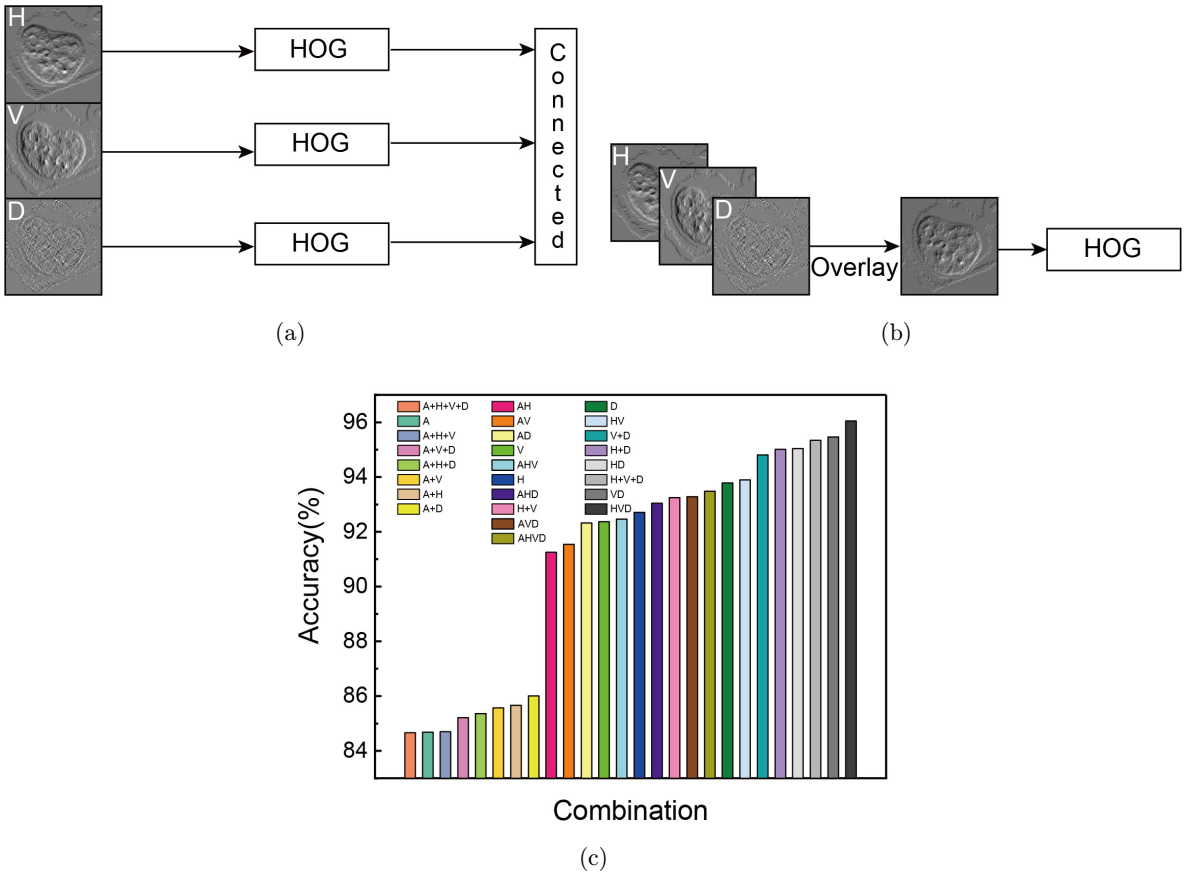

Fig. 5. Comparison of HOG feature combination modes: (a) tandem feature combination mode; (b) overlay feature combination mode; and (c) average prediction accuracies of feature combination modes.

the start of training to convergence. The HOG vectors of cells in the block were normalized to eliminate the influence of uneven gradient amplitude on prediction accuracy. To optimize the final prediction accuracy and training time, models with different cell sizes and block regions were trained to evaluate the average prediction accuracies, feature dimensions, and training times. The results are shown in Fig. 6.

As shown in Fig. 6(b), the highest prediction accuracy is achieved by the model when the cell window size is 30×30 pixels and the block contains 3×3 cell windows. Because the block size does not affect feature dimension, it is set to 3×3 cells to calculate the feature dimensions and training times of different cell sizes; results are shown in Fig. 6(a). The figure shows that as the cell size increases, the feature dimension and training time decrease. For example, when the cell size was 24×24 pixels, the training time spiked. Hence, the model has the optimal classification effect and highest time efficiency when the cell and block sizes are 30×30 pixels and 3×3 cells, respectively. Note that after wavelet decomposition, the image height and width should be halved. In setting cell parameters, the height and width must also be halved (i.e., 15×15 pixels).

As shown in Fig. 4, the nuclei of healthy cells are evenly distributed with small circular holes. When apoptosis occurs owing to chromatin aggregation, the uniformly distributed small circular holes gradually expand to form large irregular strip-shaped holes. The size of each small circular hole is approximately 30×30 pixels. When the rectangular window is set to 30×30 pixels, the edge of the small hole can be completely captured, and the interference of other edge noise occurring in the large window can be avoided. Therefore, the prediction performance of the model is optimal when the cell window size is 30×30 pixels.

3.3. *Prediction performance evaluation*

3.3.1. *Ablation experiment*

An ablation experiment was conducted to compare the prediction performance of different feature

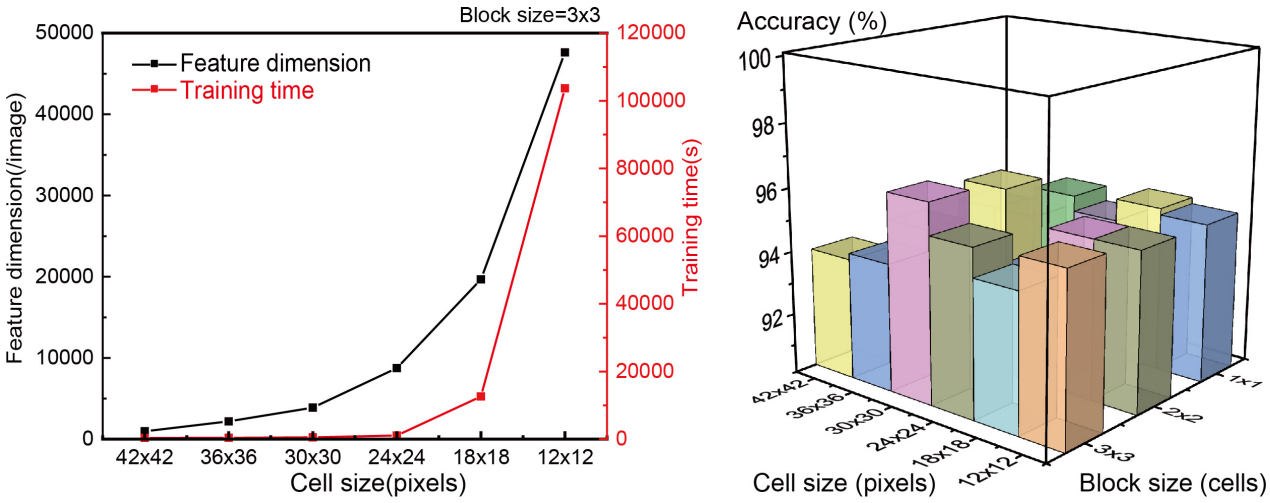

(a) (b)

Fig. 6. Model prediction performance of different cell and block sizes: (a) training time (s) and feature dimensions (per image) of different cell sizes (pixels) when block size is 3×3 (cells); (b) average prediction accuracies of different cell sizes (pixels) and block sizes (cells).

extraction methods. Table 1 summarizes the 10-fold cross-validation results of classifying apoptotic/healthy cells based on models established using different features. The table indicates that the model based on the HOG features of high-frequency wavelet coefficients (HOG–wavelet) achieves an average prediction accuracy of 95.70% with reference to the independent test dataset, and the recall rate approximates the precision rate. The $F1$-score and AUC value are also high, reaching 95.77% and 0.96, respectively.

The list in Table 2 compares the time and feature dimensions of the models based on different features. The vector dimension of HOG–wavelet is observed to be 3888, which is evidently shorter than 9801 and 30,000 (i.e., the vector dimensions of the other two models). The training time was reduced to 535.00 s; the other methods required more than 2722.10 s. Overall, the classification model based on the HOG–wavelet feature had the highest prediction accuracy and lowest cost in terms of training time.

3.3.2. *Prediction performance of various classification models*

Table 3 summarizes the prediction results for identifying apoptosis from the test data using various machine learning methods and deep learning models. Traditional feature extraction methods are trained from scratch on a same CPU (Intel(R) Core(TM) i5-4200H with 16 GB of memory capacity). Deep learning models are trained on a GPU (NVIDIA 1070Ti with 8 GB of memory capacity). In particular, we evaluated the performance of our method and MobileNetV3 Large trained with GPU and CPU, respectively. ThunderSVM library[29] was used for SVM training on GPU. For MobileNets, we use the pre-trained model from ImageNet and populate the new architecture, truncating and randomly initializing missing weights as appropriate. All convolutional layers in MobileNets are frozen during training and use batch-normalization layers with average decay of 0.99. The other deep learning models are trained from scratch. For the

Table 1. Classification performance according to various features.

Feature	Accuracy (%)	Precision (%)	Recall (%)	$F1$-score (%)	AUC
HOG–wavelet	95.70 ± 0.92	94.40 ± 1.36	97.18 ± 0.93	95.77 ± 0.90	0.96 ± 0.01
HOG	93.55 ± 0.53	90.46 ± 1.33	97.42 ± 0.85	93.80 ± 0.47	0.93 ± 0.01
Wavelet	89.97 ± 0.98	84.65 ± 1.97	97.72 ± 0.50	90.70 ± 1.06	0.90 ± 0.01

Table 2. Training time and feature dimensions of models based on various features.

Feature	Time for feature extraction (ms/image)	Feature dimension	Time for training (s)	Time for identification (ms/image)
HOG–wavelet	36.75 ± 1.59	3888	535.00 ± 51.16	0.019 ± 0.0012
HOG	57.75 ± 3.75	9801	2722.10 ± 38.05	0.025 ± 0.0010
Wavelet	28.00 ± 3.67	30,000	$10{,}907.82 \pm 73.33$	0.013 ± 0.0010

Table 3. Prediction performance of various models in identifying apoptosis.

Method	Accuracy (%)	Precision (%)	Recall (%)	$F1$-score (%)	Time for training and feature extraction (s)	AUC
HOG–wavelet	95.70 ± 0.92	94.40 ± 1.36	97.18 ± 0.93	95.77 ± 0.90	535.00 ± 51.16 (CPU) 21.95 ± 1.14 (GPU)	0.96 ± 0.01
LBP	90.25 ± 1.84	85.25 ± 2.35	97.42 ± 1.38	90.91 ± 1.62	1017.58 ± 32.00 (CPU)	0.90 ± 0.02
GLCM	87.68 ± 2.96	88.52 ± 4.10	86.70 ± 2.35	87.54 ± 2.35	796.07 ± 24.70 (CPU)	0.88 ± 0.02
MobileNetV3 Large	96.71 ± 0.55	96.13 ± 0.24	95.88 ± 0.33	96.29 ± 0.26	$26{,}494.50 \pm 56.34$ (CPU)	0.96 ± 0.01
	97.22 ± 0.37	96.79 ± 0.40	98.01 ± 0.42	97.39 ± 0.39	237.32 ± 1.60 (GPU)	0.97 ± 0.00
MobileNetV3 Small	96.59 ± 0.66	96.16 ± 0.25	97.89 ± 0.21	96.98 ± 0.22	225.25 ± 1.74 (GPU)	0.96 ± 0.00
MobileNetV2	95.54 ± 0.78	95.01 ± 0.60	96.58 ± 0.53	95.57 ± 0.58	512.01 ± 2.03 (GPU)	0.95 ± 0.01
AlexNet	88.53 ± 1.58	84.37 ± 1.58	92.89 ± 1.21	88.43 ± 1.24	402.01 ± 2.77 (GPU)	0.88 ± 0.01
ResNet-18	93.78 ± 0.64	92.96 ± 0.58	95.55 ± 0.88	94.24 ± 0.70	707.82 ± 5.91 (GPU)	0.94 ± 0.01

deep learning models, training is done using stochastic gradient descent optimizer with 0.9 momentum and mini-batches of size 32. The initial learning rate is set to 0.01, and is divide by 10 for every three epochs. The model is trained to convergence, where MobileNets, AlexNet and ResNet-18 were trained with 3, 6 and 6 epoches, respectively. We use a dropout rate of 0.8, and an $L2$-regularization weight decay of 10^{-3}. Cross-entropy is used as the loss function. We perform data augmentation by randomly rotating, scaling, flipping and contrasting images. The training time is measured by GPU/CPU running time from the start of training until the model converges.

The table indicates that the proposed HOG–wavelet method achieves the higher accuracy compared with the traditional feature extraction method. Compared with MobileNetV3 Large, the deep learning model with the best performance in the table, our method reduces training time significant. Specifically, the training time is shortened from 26,494.50 s to 535 s on CPU and from 237.32 s to 21.95 s on GPU, while the accuracy is only reduced by 1.01% and 1.52%.

4. Discussion

Different from current methods, which are based on morphological parameter features, our method considers both gradient amplitude and orientation distribution. Thus, the proposed method more completely describes the cell nucleus texture and edge orientation. Because the method is based on textures and edges, it can be facilely applied to other contexts where distinct edge texture changes can be identified by simply tuning the HOG parameter.

This paper proposes a feature combination method in which HOG features are extracted from the high-frequency coefficients of different directions and then connected in series. Instead of directly calculating the HOG features, the proposed technique extracts distinct edge texture. Moreover, downsampling during wavelet decomposition has been found to reduce the image resolution, thus reducing the dimensions of the HOG feature vector. However, experimental results show that the prediction accuracy of our method is close to that of the deep learning model in a short training time on both GPU and CPU. This allows us to obtain the model in a short time using only a CPU on a system with low GPU performance, thus greatly reduce hardware cost.

Because the method fundamentally describes the morphology of the nucleus based on the texture of its edges, when the raw image is extremely fuzzy, correctly extracting the edge with the gradient is difficult. This affects the extraction of the HOG vector and the final identification accuracy. Therefore, the inclusion of appropriate preprocessing, such as image deblurring and image enhancement, is necessary before feature extraction based on the actual situation. In addition, the fluorescence image contains rich feature information (except edge features). Accordingly, in the future, we intend to investigate other feature combinations to obtain better recognition accuracy in fuzzy images.

5. Conclusion

In this study, an apoptosis identification method for the fluorescence imaging of the nucleus based on the HOG features of high-frequency wavelet coefficients was successfully established. The study results showed that the HOG–wavelet classification model has great identification performance. The average prediction accuracy with reference to test data reached 95.70% within a short training time. We expect our study results to benefit the research on large-scale apoptotic cell analysis and biological applications.

Conflicts of Interest

The authors have no conflicts of interest relevant to this article.

Acknowledgments

This work is supported by the Key Project of the National Natural Science Foundation of China (Grant Number 62135003), the Science and Technology Program of Guangzhou (Grant No. 202201010704) and Special Carrier Program of Qingyuan Hitech Industrial Development Zone.

References

1. R. S. Y. Wong, "Apoptosis in cancer: From pathogenesis to treatment," *J. Exp. Clin. Cancer Res.* **30**(1), 87 (2011).
2. G. Kroemer, L. Galluzzi, P. Vandenabeele, J. Abrams, E. S. Alnemri, E. H. Baehrecke, M. V. Blagosklonny, W. S. El-Deiry, P. Golstein, D. R. Green, M. Hengartner, R. A. Knight, S. Kumar, S. A. Lipton, W. Malorni, G. Nuñez, M. E. Peter, J. Tschopp, J. Yuan, M. Piacentini, B. Zhivotovsky, G. Melino, "Classification of cell death: Recommendations of the nomenclature committee on cell death 2009," *Cell Death Differ.* **16**(1), 3–11 (2009).
3. G. Majno, I. Joris, "Apoptosis, oncosis, and necrosis: An overview of cell death," *Am. J. Pathol.* **146**(1), 3–15 (1995).
4. J.-W. Oh, Y. J. Oh, S. Han, N.-G. Her, D.-H. Nam, "High-content analysis-based sensitivity prediction and novel therapeutics screening for c-Met-addicted glioblastoma," *Cancers* **13**(3), 372 (2021).
5. J. A. Marwick, R. J. R. Elliott, J. Longden, A. Makda, N. Hirani, K. Dhaliwal, J. C. Dawson, N. O. Carragher, "Application of a high-content screening assay utilizing primary human lung fibroblasts to identify antifibrotic drugs for rapid repurposing in COVID-19 patients," *SLAS Discov. Adv. Sci. Drug Discov.* **26**(9), 1091–1106 (2021).
6. M. Esner, F. Meyenhofer, M. Bickle, "Live-cell high content screening in drug development," *Methods Mol. Biol.* **1683**, 149–164 (2018).
7. D. L. Taylor, "Past, present, and future of high content screening and the field of cellomics," *Methods Mol. Biol.* **356**, 3–18 (2007).
8. Z. Yang, J. Shang, C. Liu, J. Zhang, Y. Liang, "Identification of oral squamous cell carcinoma in optical coherence tomography images based on texture features," *J. Innov. Opt. Health Sci.* **14**(1), 2140001 (2021).
9. S. H. Jo, Y. Kim, Y. B. Lee, S. S. Oh, J. R. Choi, "A comparative study on machine learning-based classification to find photothrombotic lesion in histological rabbit brain images," *J. Innov. Opt. Health Sci.* **14**(6), 1–9 (2021).
10. J. Ker, L. Wang, J. Rao, T. Lim, "Deep learning applications in medical image analysis," *IEEE Access* **6**, 9375–9389 (2018).
11. A. Howard, M. Sandler, G. Chu, L.-C. Chen, B. Chen, M. Tan, W. Wang, Y. Zhu, R. Pang, V. Vasudevan, "Searching for MobileNetV3," *Proc. IEEE/CVF Int. Conf. Computer Vision*, pp. 1314–1324, IEEE Computer Society (2019).
12. A. Krizhevsky, I. Sutskever, G. E. Hinton, "Imagenet classification with deep convolutional neural networks," *Commun. ACM* **60**(6), 84–90 (2017).
13. K. He, X. Zhang, S. Ren, J. Sun, "Deep residual learning for image recognition," *Proc. 2016 IEEE Conf. Computer Vision and Pattern Recognition (CVPR)*, pp. 770–778, IEEE Computer Society (2016).

14. G. Zhao, T. Ahonen, J. Matas, M. Pietikainen, "Rotation-invariant image and video description with local binary pattern features," *IEEE Trans. Image Process.* **21**(4), 1465–1477 (2012).
15. R. M. Haralick, K. Shanmugam, I. Dinstein, "Textural features for image classification," *IEEE Trans. Syst. Man Cybern.* **SMC-3**(6), 610–621 (1973).
16. A. Mobiny, H. Lu, H. V. Nguyen, B. Roysam, N. Varadarajan, "Automated classification of apoptosis in phase contrast microscopy using capsule network," *IEEE Trans. Med. Imaging* **39**(1), 1–10 (2020).
17. J. Feng, T. Feng, C. Yang, W. Wang, Y. Sa, Y. Feng, "Feasibility study of stain-free classification of cell apoptosis based on diffraction imaging flow cytometry and supervised machine learning techniques," *Apoptosis* **23**(5–6), 290–298 (2018).
18. C. Rens, T. Shapira, S. Peña-Diaz, J. D. Chao, T. Pfeifer, Y. Av-Gay, "Apoptosis assessment in high-content and high-throughput screening assays," *Biotechniques* **70**(6), 309–318 (2021).
19. C. M. Garvey, E. Spiller, D. Lindsay, C. T. Chiang, N. C. Choi, D. B. Agus, P. Mallick, J. Foo, S. M. Mumenthaler, "A high-content image-based method for quantitatively studying context-dependent cell population dynamics," *Sci. Rep.* **6**(July), 1–12 (2016).
20. U. Anilkumar, P. Weisova, J. Schmid, T. Bernas, H. J. Huber, H. Düssmann, N. M. Connolly, J. H. Prehn, "Defining external factors that determine neuronal survival, apoptosis and necrosis during excitotoxic injury using a high content screening imaging platform," *PLoS One* **12**(11), 1–19 (2017).
21. J. Quinlan, "Induction of decision trees," *Mach. Learn.* **1**(1), 81–106 (1986).
22. N. Dalal, B. Triggs, "Histograms of oriented gradients for human detection," *2013 IEEE Conf. Computer Vision and Pattern Recognition*, pp. 886–893, IEEE Computer Society (2005).
23. I. Haritaoglu, D. Harwood, L. S. Davis, "W4: Real-time surveillance of people and their activities," *IEEE Trans. Pattern Anal. Mach. Intell.* **22**(8), 809–830 (2000).
24. N. Otsu, "A threshold selection method from gray-level histograms," *IEEE Trans. Syst. Man Cybern.* **9**(1), 62–66 (1979).
25. J. A. M. Sidey-Gibbons, C. J. Sidey-Gibbons, "Machine learning in medicine: A practical introduction," *BMC Med. Res. Methodol.* **19**(1), 64 (2019).
26. S. Mallat, "A theory for multiresolution signal decomposition: The wavelet representation," *IEEE Trans. Pattern Anal. Mach. Intell.* **11**(7), 674–693 (1989).
27. J. Cervantes, F. Garcia-Lamont, L. Rodríguez-Mazahua, A. Lopez, "A comprehensive survey on support vector machine classification: Applications, challenges and trends," *Neurocomputing* **408**, 189–215 (2020).
28. B. Goyal, A. Dogra, S. Agrawal, B. Sohi, A. Sharma, "Image denoising review: From classical to state-of-the-art approaches," *Inf. Fusion* **55**, 220–244 (2020).
29. Z. Wen, J. Shi, Q. Li, B. He, J. Chen, "ThunderSVM: A fast SVM library on GPUs and CPUs," *J. Mach. Learn. Res.* **19**(1), 797–801 (2018).